Journal of Materials Chemistry A

Synthesis, band structure and photocatalytic property of Sillén–Aurivillius oxychlorides $BaBi_5Ti_3O_{14}Cl$, $Ba_2Bi_5Ti_4O_{17}Cl$ and $Ba_3Bi_5Ti_5O_{20}Cl$ with triple-, quadruple- and quintuple-perovskite layers

Journal:	*Journal of Materials Chemistry A*
Manuscript ID	TA-ART-12-2020-012550.R1
Article Type:	Paper
Date Submitted by the Author:	12-Feb-2021
Complete List of Authors:	Ozaki, Daichi; Kyoto University, Energy and Hydrocarbon Chemistry Suzuki, Hajime; Kyoto University, Ogawa, Kanta; Kyoto University Faculty of Engineering Graduate School of Engineering, The Department of Energy and Hydrocarbon Chemistry Sakamoto, Ryota; The University of Tokyo, Department of Chemistry, Graduate School of Science Inaguma, Yoshiyuki ; Gakushuin University, Department of Cheistry, Faculty of Science Nakashima, Kouichi; Ibaraki Daigaku Kogakubu, Tomita, Osamu; Kyoto University, Graduate School of Engineering Kageyama, Hiroshi; Kyoto University, Department of Energy and Hydrocarbon Chemistry Abe, Ryu; Kyoto University, Graduate School of Engineeing

ARTICLE

Synthesis, band structure and photocatalytic property of Sillén–Aurivillius oxychlorides $BaBi_5Ti_3O_{14}Cl$, $Ba_2Bi_5Ti_4O_{17}Cl$ and $Ba_3Bi_5Ti_5O_{20}Cl$ with triple-, quadruple- and quintuple-perovskite layers

Received 00th January 20xx,
Accepted 00th January 20xx

DOI: 10.1039/x0xx00000x

Daichi Ozaki,[ab] Hajime Suzuki,[a] Kanta Ogawa,[ab] Ryota Sakamoto,[a] Yoshiyuki Inaguma,[c] Kouichi Nakashima,[d] Osamu Tomita,[a] Hiroshi Kageyama*[a] and Ryu Abe*[ab]

Sillén–Aurivillius layered oxyhalides with a single-, double- and triple-perovskite slabs (n = 1–3) are promising visible-light-driven photocatalysts for water splitting with different behaviors observed depending on n. However, there was no report on the photocatalytic activity of $n \geq 4$ phases. Here we report three new oxychlorides $BaBi_5Ti_3O_{14}Cl$, $Ba_2Bi_5Ti_4O_{17}Cl$ and $Ba_3Bi_5Ti_5O_{20}Cl$, respectively, with triple-, quadruple- and quintuple-perovskite layers. The synthesis of these phases involve a "bricklaying" synthesis, where a plain perovskite $BaTiO_3$, a Sillén phase $BaBiO_2Cl$ and Aurivillius phases $Bi_4Ti_3O_{12}$, $BaBi_4Ti_4O_{15}$, $Ba_2Bi_4Ti_5O_{18}$ were used as building blocks. The present Sillén–Aurivillius oxychlorides have appropriate valence and conduction band levels for visible-light-induced water splitting. DFT calculation for $BaBi_5Ti_3O_{14}Cl$ (n = 3) and $Ba_3Bi_5Ti_5O_{20}Cl$ (n = 5) indicates their valence and conduction bands are separated spatially on the perovskite and fluorite layers, respectively. The photocatalytic activity of the three Sillén–Aurivillius oxychlorides is enhanced with increasing the number of the perovskite layers.

Introduction

Photocatalytic water splitting that utilizes solar energy is regarded as potential technology to produce hydrogen as a next energy carrier.[1–7] In order to allow this technology to play a major role in the steady supply of hydrogen, efficient and stable semiconductor photocatalysts harvesting a broader range of the sunlight spectrum are required. Hence, intensive effort has been devoted to various semiconductors such as metal oxides, (oxy)nitrides, (oxy)sulfides and oxyhalides.[7,8]

Bismuth-based oxyhalides have attracted great attention in various research fields,[9–13] such as photocatalysis.[14–16] Among these materials, layered perovskite oxyhalides Bi_4MO_8X (M = Nb, Ta; X = Cl, Br) are promising photocatalysts for water splitting under visible light.[17,18] They correspond to the n = 1 type of Sillén–Aurivillius phases with a general formula of $(Bi_2O_2)_2X(A_{n-1}M_nO_{3n+1})$, where n represents the number of perovskite layers. Bi_4MO_8X possess a valence band maximum (VBM; +2.3–2.5 V vs. SHE) more negative than conventional metal oxides (ca. +3.0 V), which endows Bi_4MO_8X with visible-light-absorbability, as well as band levels appropriate for both water oxidation and reduction.

Sillén–Aurivillius phases consist of halide, fluorite and perovskite slabs; selective cation and/or anion substitution for the layers may provide broad structural variations, changing their optical and electrochemical properties.[19–21] The number of perovskite layers, n, is considered to be an important parameter to control and improve the photocatalytic activity due to a wide range of cation choices, as our previous reports on n = 2 and 3 systems.[22–24] For n = 2, we demonstrated that the band levels of $AA'Bi_3M_2O_{11}Cl$ (A, A' = Sr, Ba, Pb, Bi; M = Ti, Nb, Ta) can be engineered systematically by cation substitution.[22] For example, the valence band maxima (VBM) of Pb derivatives shift negatively, which is derived from a contribution of Pb-6s that hybridizes with O-2p. A contrasting behaviour is found in n = 3 $Bi_5MTi_3O_{14}Cl$ (M = Pb, Sr) with their VBM similar to each other (+2.2–2.3 V),[24] which is surprising because Pb is known to effectively raise the VBM.[25–28] We deduce that the VBM of $Bi_5SrTi_3O_{14}Cl$ results from strong interaction among O-2p and Bi-6s orbitals in the perovskite slab; $Bi_5SrTi_3O_{14}Cl$ includes Bi^{3+} as a major component at the A site of the perovskite layer, while this site is occupied by divalent cations (e.g., Ba^{2+}, Sr^{2+}) in the n = 2 phases.[22,29,30] Increasing the number of the perovskite layers offers a platform for systematic investigation of various factors related to photocatalytic function. To the best of our knowledge, however, there is no report on photocatalytic properties of the $n \geq 4$ phases.

In the present study, we report on the synthesis, crystal structure, band configuration, and photocatalytic property of the n = 4 and 5 types of Sillén–Aurivillius phases. Following our recent finding that n = 3 $Bi_5SrTi_3O_{14}Cl$ exhibits higher photocatalytic activity than an analogue $Bi_5PbTi_3O_{14}Cl$,[24] we set $Bi_5SrTi_3O_{14}Cl$ as one of the starting materials for further exploration of n = 4, 5 phases. In addition to that, Ba-containing

[a] Department of Energy and Hydrocarbon Chemistry, Graduate School of Engineering, Katsura, Kyoto University, Nishikyo-ku, Kyoto 615-8510, Japan
[b] AIST-Kyoto University Chemical Energy Materials Open Innovation Laboratory (ChEM-OIL), National Institute of Advanced Industrial Science and Technology (AIST), Yoshida, Sakyo-ku, Kyoto 606-8501, Japan
[c] Department of Chemistry, Faculty of Science, Gakushuin University, Toshima-ku, Tokyo 171-8588, Japan
[d] Department of Materials Science and Engineering, Graduate School of Science and Engineering, Ibaraki University, 4-12-1, Nakanarusawa, Hitachi, Ibaraki 316-8511, Japan
†Electronic Supplementary Information (ESI) available: See DOI: 10.1039/x0xx00000x
*E-mail: kage@scl.kyoto-u.ac.jp (H.K.), ryu-abe@scl.kyoto-u.ac.jp (R.A.)

analogues with n = 3–5 are explored: For the n = 2 type, the Ba-based phases possess narrower bandgaps than the Sr counterparts (e.g., $Ba_2Bi_3Ta_2O_{11}Cl$ (2.57 eV); $Sr_2Bi_3Ta_2O_{11}Cl$ (2.86 eV).[22]

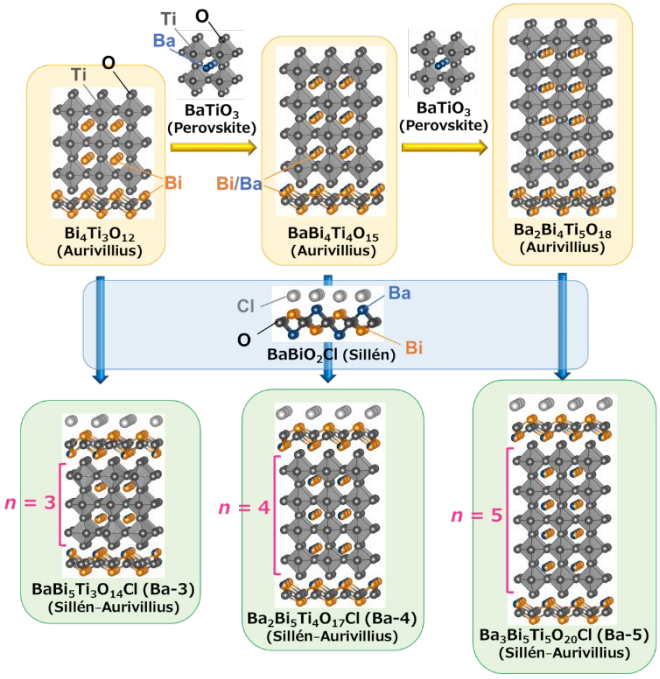

Fig. 1 An illustration of the bricklaying synthesis for Sillén–Aurivillius phases $BaBi_5Ti_3O_{14}Cl$ (**Ba-3**), $Ba_2Bi_5Ti_4O_{17}Cl$ (**Ba-4**) and $Ba_3Bi_5Ti_5O_{20}Cl$ (**Ba-5**) as the representatives.

Results and discussion

Synthesis strategy

In general, the synthesis of layered perovskites requires high-temperature calcination with increasing n (e.g., 1100 °C for n = 5 Aurivillius phase $Ba_2Bi_4Ti_5O_{18}$).[31] On the other hand, oxyhalides suffer from volatilization of halogen species during such a high-temperature treatment, which forms impurity phases. In order to solve the trade-off and obtain pure phases, we employed a "bricklaying" synthesis to access thicker-layered Sillén-Aurivillius oxychlorides with n = 3–5, which consists of two reaction processes (Fig.1). The first is a reaction between an Aurivillius phase $(Bi_2O_2)(A_{n-1}Ti_nO_{3n+1})$ with n = k and a plain perovskite $ATiO_3$ (A = Sr, Ba) to form an Aurivillius phase with n = k+1 (k ≥ 3)(e.g., $BaBi_4Ti_4O_{15}$ (n = 4) + $BaTiO_3$ ⟶ $Ba_2Bi_4Ti_5O_{18}$ (n = 5); see yellow arrows in Fig. 1). Such a reaction is known in other layered perovskites such as Dion–Jacobson phases (e.g., $RbCa_2Nb_3O_{10}$ (n = 3) + $NaNbO_3$ ⟶ $RbCa_2NaNb_4O_{13}$ (n = 4)).[32] The second is a reaction between a Sillén phase $ABiO_2Cl$ and the pre-synthesized Aurivillius phase with n = k+1 to form a Sillén–Aurivillius phase with n = k+1 (e.g., $BaBiO_2Cl$ + $Ba_2Bi_4Ti_5O_{18}$ ⟶ $Ba_3Bi_5Ti_5O_{20}Cl$; see a blue arrow in Fig. 1), the concept of which was first proposed by Aurivillius.[33] Sillén and Aurivillius phases are structurally compatible with respect to the in-plane cell dimension, so this reaction can offer purer Sillén–Aurivillius phases than a conventional method.[29,30,34]

Synthesis

Sr-containing compounds. X-ray diffraction (XRD) patterns confirmed the pure-phase formation of precursor samples: a Sillén phase $SrBiO_2Cl$ and Aurivillius phases $Bi_4Ti_3O_{12}$, $SrBi_4Ti_4O_{15}$ and $Sr_2Bi_4Ti_5O_{18}$ (Fig. S1). As shown in Fig. S2, the n = 3 $Bi_5SrTi_3O_{14}Cl$ was successfully prepared as our previous report.[24] However, XRD patterns for the n = 4, 5 phases indicates imperfect crystallization; attempts to synthesize n = 4, 5 types of Sr-containing compounds were unsuccessful at this synthesis condition (900 °C for 20 h). Further optimization of it may give these phases in the future work.

Ba-containing compounds. Fig. S3 shows XRD patterns of precursor samples of a Sillén phase $BaBiO_2Cl$ and Aurivillius phases $BaBi_4Ti_4O_{15}$ and $Ba_2Bi_4Ti_5O_{18}$, which confirmed they were pure phases. Ba-containing compounds, n = 3 $BaBi_5Ti_3O_{14}Cl$ (**Ba-3**), n = 4 $Ba_2Bi_5Ti_4O_{17}Cl$ (**Ba-4**) and n = 5 $Ba_3Bi_5Ti_5O_{20}Cl$ (**Ba-5**), were synthesized by the bricklaying synthesis. The XRD pattern of **Ba-3** was similar to that of Sr analogue $Bi_5SrTi_3O_{14}Cl$,[24] which shows that the target **Ba-3** phase was obtained (Fig. S4). The **Ba-4** and **Ba-5** were also successfully prepared.

SEM images in Fig. S5 show that **Ba-3, Ba-4** and **Ba-5** have similar particle sizes (1–5 μm). Their specific surface areas are not quite different (**Ba-3**: 1.8 m^2/g, **Ba-4**: 3.6 m^2/g, **Ba-5**: 1.9 m^2/g). Fig. S6–S8 show extreme ultra-violet light excited photoelectron spectroscopy (EUPS)[35,36] spectra, yielding Cl/Bi ratios at the surface of 0.19, 0.18 and 0.21 for **Ba-3**, **Ba-4** and **Ba-5**, respectively. These values are agreement with the ideal value Cl/Bi = 0.2 from each chemical formula.

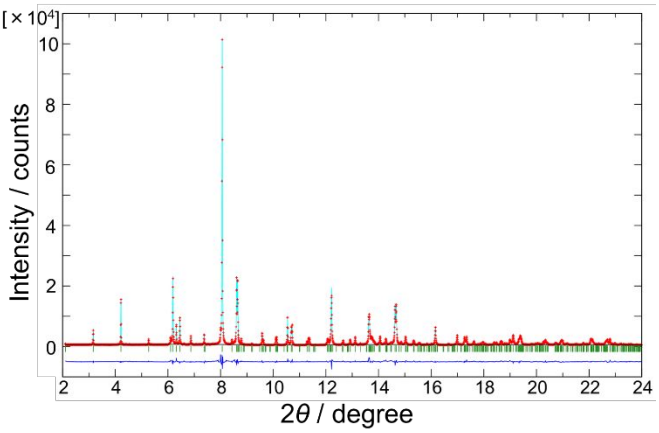

Fig. 2 Final Rietveld plot for $BaBi_5Ti_3O_{14}Cl$ (**Ba-3**) using the SXRD pattern collected at room temperature; R_p = 0.0630, R_{wp} = 0.0867, R_B = 0.0540, R_F = 0.0415, χ^2 = 3.075.

Crystal structure analysis

$BaBi_5Ti_3O_{14}Cl$ (Ba-3). Rietveld refinement for **Ba-3** was carried out in combination of neutron powder diffraction (NPD) and synchrotron powder X-ray diffraction (SXRD) patterns collected at room temperature. The NPD pattern was mainly used to refine fractional coordinates and isotropic atomic displacement parameters of anions (i.e., O and Cl). Refinements of other structure parameters (i.e., occupancies, fractional coordinates and isotropic atomic displacement parameters of cations and lattice parameters) were carried out using the SXRD pattern. All the diffraction peaks within 2θ = 2–24° were indexed using the orthorhombic system, excepting small impurity peaks. Since **Ba-3** is SHG active (Fig. S9), it should have a non-centrosymmetric space group. Based on this result, the reflection conditions in the SXRD pattern uniquely gives $P2an$ (#30), the same space group for n = 3 $Bi_5MTi_3O_{14}Cl$ (M = Pb, Sr).[24,37] The final Rietveld plot of the SXRD and NPD patterns are displayed in Fig. 2 and Fig. S10, respectively (see also Tables S1 and S2). Reliability

factors for the SXRD pattern converged to R_p = 0.0630, R_{wp} = 0.0867, R_B = 0.0540, R_F = 0.0415, χ^2 = 3.075 and ones for the NPD pattern converged to R_p = 0.0754, R_{wp} = 0.0966, R_B = 0.0713, R_F = 0.0310, χ^2 = 3.126.

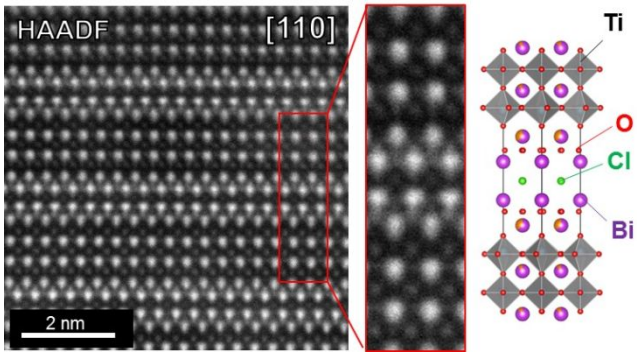

Fig. 3 HAADF-STEM images of $Bi_5BaTi_3O_{14}Cl$ (**Ba-3**) in the direction of [110].

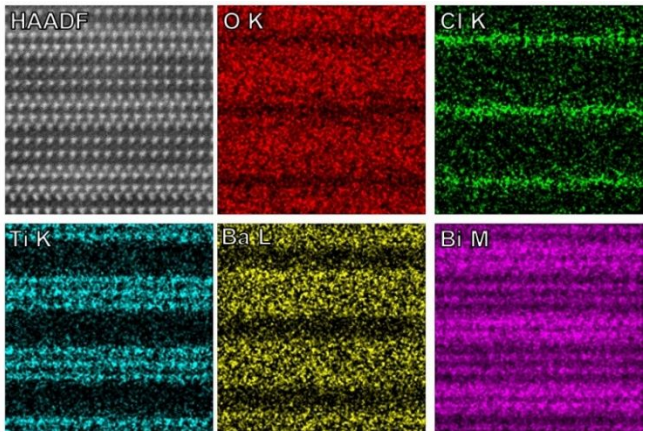

Fig. 4 HAADF-STEM image and EDX elemental maps of $BaBi_5Ti_3O_{14}Cl$ (**Ba-3**) in the direction of [110].

Scanning transmission electron microscopy (STEM) observation was performed for **Ba-3**. Fig. 3 shows high-angle annular dark field STEM (HAADF-STEM) and images in the direction of [110] (see Fig. S11 for an annular bright-field STEM (ABF-STEM) image). A clear periodical atomic arrangement corresponding to the refined crystal structure was observed. Fig. 4 shows elemental maps of **Ba-3** in the direction of [110] measured by energy-dispersive X-ray spectroscopy (EDX). The elemental maps show the intergrowth of fluorite, perovskite and halide layers, further supporting the successful synthesis of **Ba-3**.

$Ba_2Bi_5Ti_4O_{17}Cl$ (Ba-4) and $Ba_3Bi_5Ti_5O_{20}Cl$ (Ba-5). The SXRD for **Ba-4** and **Ba-5** in the range of 2θ = 2–24° were indexed using the tetragonal unit cells, without systematic absences of diffraction peaks. Thus, we adopted for Rietveld refinement the highest symmetry space group *P*4/*mmm* (#123) among possible space groups, the results of which are shown in Fig. S12 and Fig. S13 for **Ba-4** and **Ba-5**, respectively. Obtained reliability factors are reasonable (for **Ba-4**, R_p = 0.1184, R_{wp} = 0.1761, R_B = 0.0620, R_F = 0.0526, χ^2 = 2.884, and for **Ba-5**, R_p = 0.0944, R_{wp} = 0.1437, R_B = 0.0468, R_F = 0.0365, χ^2 = 3.609). The final refined structure parameters and bond lengths are summarized in Tables S3–S5.

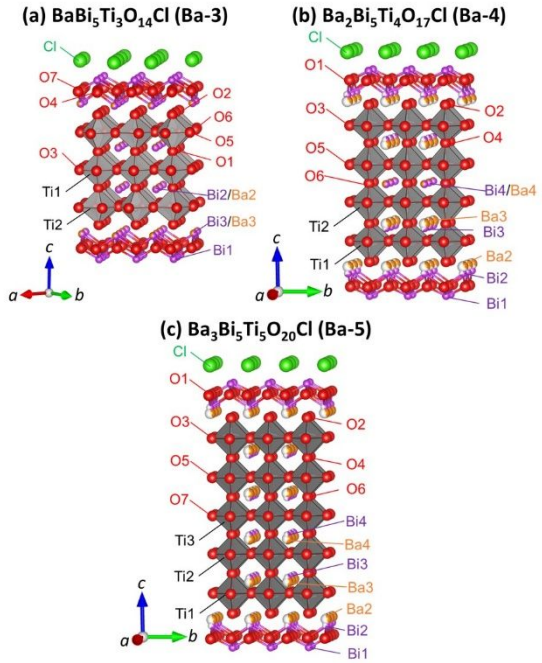

Fig. 5 Refined crystal structures of (a) $BaBi_5Ti_3O_{14}Cl$ (**Ba-3**), (b) $Ba_2Bi_5Ti_4O_{17}Cl$ (**Ba-4**) and (c) $Ba_3Bi_5Ti_5O_{20}Cl$ (**Ba-5**).

The refined crystal structures of **Ba-3**, **Ba-4** and **Ba-5** are displayed in Fig. 5. The present compounds have three or four Bi/Ba sites in their unit cells. The Bi/Ba1 sites being next to the halide layers were fully occupied by Bi^{3+} without Ba^{2+} (see Table 1). In HAADF-STEM of **Ba-3** (Fig. 6), heavier atoms look brighter. Therefore, the fact that the extracted brightness of Bi/Ba sites was ordered as Bi/Ba1 > Bi/Ba3 > Bi/Ba2 supports the preferential occupation of the Bi/Ba1 site by Bi^{3+}. Such a preferential occupation has been also known in *n* = 2, 3 type of Sillén–Aurivillius phases.[22,24] The Bi^{3+} cations have $6s^2$ lone pairs, which become stereochemically active when interacted with O-2p orbitals based on the revised lone pair model.[38] In general, lone pair cations such as Bi^{3+} and Pb^{2+} tend to occupy the cation sites in the fluorite layers rather than those in the perovskite layers due to a preference for pyramidal coordination, as is well known in the related Aurivillius oxides.[39] Additionally, in the

Table 1 Final refined occupancies of each Bi/Ba site and lattice parameters of $BaBi_5Ti_3O_{14}Cl$ (**Ba-3**), $Ba_2Bi_5Ti_4O_{17}Cl$ (**Ba-4**) and $Ba_3Bi_5Ti_5O_{20}Cl$ (**Ba-5**)

Compound	*n*	Bi/Ba1	Bi/Ba2	Bi/Ba3	Bi/Ba4	*a* / Å	*b* / Å	*c* / Å
$BaBi_5Ti_3O_{14}Cl$	3	Bi: 1[a]	Bi: 0.874(2) Ba: 0.126(2)	Bi: 0.626(2) Ba: 0.374(2)	-	5.50525(6)	5.48057(5)	22.4870(2)
$Ba_2Bi_5Ti_4O_{17}Cl$	4	Bi: 1[a]	Bi: 0.670(3) Ba: 0.330(3)	Bi: 0.574(3) Ba: 0.426(3)	Bi: 0.512(3) Ba: 0.488(3)	5.53008(4)[b]	5.53008(4)[b]	26.8125(4)
$Ba_3Bi_5Ti_5O_{20}Cl$	5	Bi: 1[a]	Bi: 0.573(4) Ba: 0.427(4)	Bi: 0.489(4) Ba: 0.511(4)	Bi: 0.438(4) Ba: 0.562(4)	5.54423(4)[c]	5.54423(4)[c]	30.9881(7)

[a]Fixed during refinement. [b]True value: 3.91036(4) (= $a/\sqrt{2}$). [c]True value: 3.92036(4) (= $a/\sqrt{2}$).

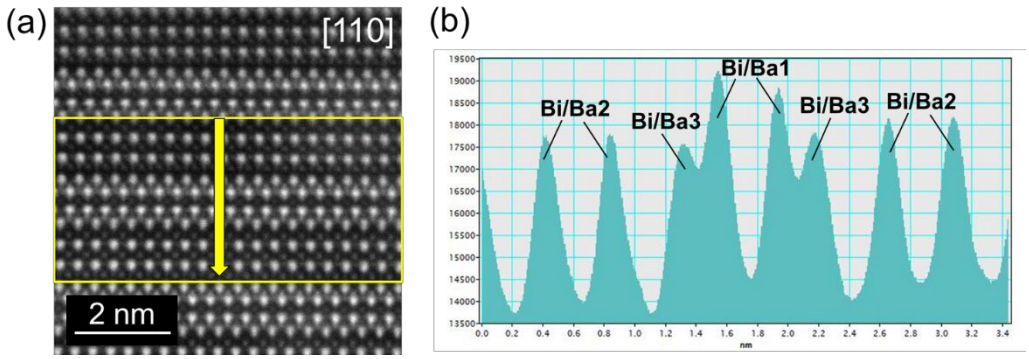

Fig. 6 (a) HAADF-STEM image of $BaBi_5Ti_3O_{14}Cl$ (**Ba-3**) in the direction of [110] and (b) the extracted brightness profile along the yellow arrow.

present oxyhalides, one side of the fluorite layer contacts with the halide layer, being more spacious than another side which contacts with the perovskite layer. Thus, it is understandable that Bi^{3+} preferentially occupies the more spacious site to stabilize the stereochemically active $6s^2$ lone pairs due to smaller electrostatic repulsion. In addition, in the related layered oxyhalides such as Bi_4MO_8X and $PbBiO_2Cl$, Bi^{3+} and Pb^{2+} cations being next to the halide layers could interact with each other across the halide layers.[40,41] Possibly, the interaction also relates with the occupancies of Bi/Ba1 sites.

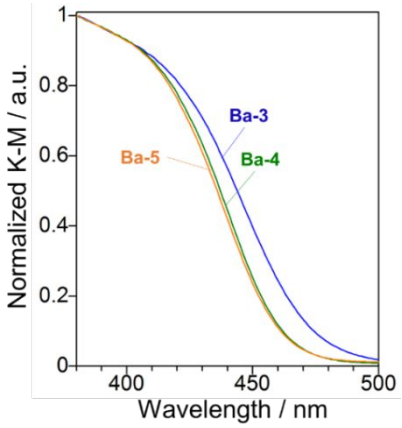

Fig.7 UV-visible diffuse reflectance spectra of $BaBi_5Ti_3O_{14}Cl$ (**Ba-3**), $Ba_2Bi_5Ti_4O_{17}Cl$ (**Ba-4**) and $Ba_3Bi_5Ti_5O_{20}Cl$ (**Ba-5**).

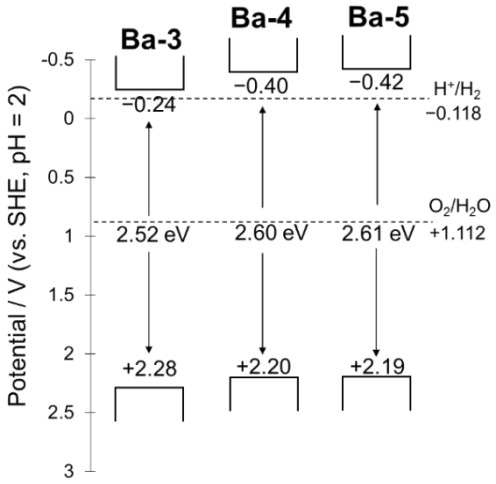

Fig. 8 Band levels of $BaBi_5Ti_3O_{14}Cl$ (**Ba-3**), $Ba_2Bi_5Ti_4O_{17}Cl$ (**Ba-4**) and $Ba_3Bi_5Ti_5O_{20}Cl$ (**Ba-5**).

The increase in the number of the perovskite layers from **Ba-3**, **Ba-4** to **Ba-5** leads to the expansion of the *c*-axis, which is obvious (see Table 1). We additionally observed a slight expansion of the in-plane axis due to the increasing content of Ba^{2+} with larger ionic radius (142 pm) than Bi^{3+} (117 pm)[42] Considering the multiplicity and the occupancy of sites, Ba^{2+} accounts for 13%, 41% and 54% of the *A* sites in the perovskite layers (i.e., Bi/Ba3, Bi/Ba4 sites) in **Ba-3**, **Ba-4** and **Ba-5**, respectively, whereas the percentage in the fluorite layers (i.e., Bi/Ba1, Bi/Ba2) are 19%, 16% and 21%, respectively. Thus, the expansion of the in-plane axis should be derived from the enlargement of the perovskite layers.

Light absorption property

Fig. 7 shows UV-visible diffuse reflectance spectra of **Ba-3**, **Ba-4** and **Ba-5**, whose absorption edges are 475 nm, 462 nm, 461 nm, respectively. Each bandgap energy was estimated to 2.52 eV, 2.60 eV and 2.61 eV by Tauc plots (Fig. S14). The bandgap energy of **Ba-3** (2.52 eV) is quite similar to that of $n = 3$ type of Sr analogue $Bi_5SrTi_3O_{14}Cl$ (2.54 eV),[24] which is different to the cases of $n = 2$ phases where cation-replacement of Sr^{2+} by Ba^{2+} makes the bandgap narrower (e.g., $Sr_2Bi_3Ta_2O_{11}Cl$ (2.86 eV) and $Ba_2Bi_3Ta_2O_{11}Cl$ (2.57 eV)).[22] Mott–Schottky plots were collected to determine flat band potentials (Fig. S15). By regarding the flat band potentials as conduction band minima (CBM), the band levels were estimated (Fig. 8). As seen in Fig. 8, **Ba-3**, **Ba-4** and **Ba-5** possess appropriate band levels for visible-light-induced water splitting, and both VBM and CBM of **Ba-4** and **Ba-5** were

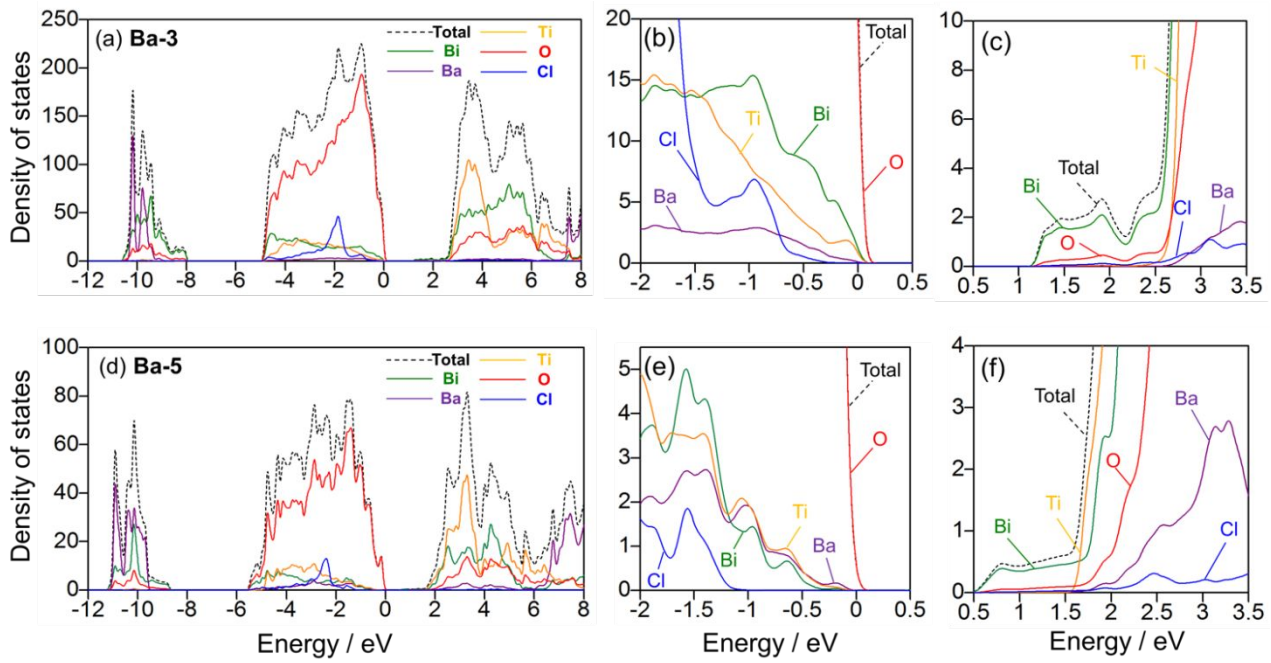

Fig. 9 DOS and PDOS of $BaBi_5Ti_3O_{14}Cl$ (**Ba-3**) and $Ba_3Bi_5Ti_5O_{20}Cl$ (**Ba-5**). (a) The whole range, (b) around the VBM and (c) CBM of **Ba-3**. (d) The whole range, (e) around the VBM and (f) CBM of **Ba-5**.

slightly shifted negative as compared to those of **Ba-3**. Note that the degrees of the CBM shifts were slightly larger than those of the VBM, so the widening bandgap is mainly derived from the shift of the CBM.

DFT calculation

Partial density of states (PDOS) was obtained based on the density functional theory (DFT) calculation using the generalized gradient approximation (GGA) with Perdew–Brurke–Ernzerhof (PBE) functional. For **Ba-3** and **Ba-5**, we built structural models reflecting the refined occupancy in Table 1, with 192 and 68-atom supercells, respectively (Fig. S16). The calculation for **Ba-4** was not conducted due to a heavier calculation cost to with a 232-atom supercell.

The calculated and experimental lattice parameters of **Ba-3** and **Ba-5** are compared in Table S6. The calculated lattice parameters are larger than the experimental values by ~2.4%, which is a well-known overestimation in the GGA-PBE functional. The calculated band gaps for **Ba-3** and **Ba-5** are 1.20 eV and 0.55 eV, respectively, which are underestimated to be −52.4% and −78.9% compared to the experimental values 2.52 eV and 2.61 eV (Table S7). The experimental band gap of **Ba-5** is larger than that of **Ba-3**, while the calculated band gaps exhibit the opposite trend. Such a disagreement may be derived from a standard error of the GGA-PBE functional, as seen in other Ti-based oxides.[43]

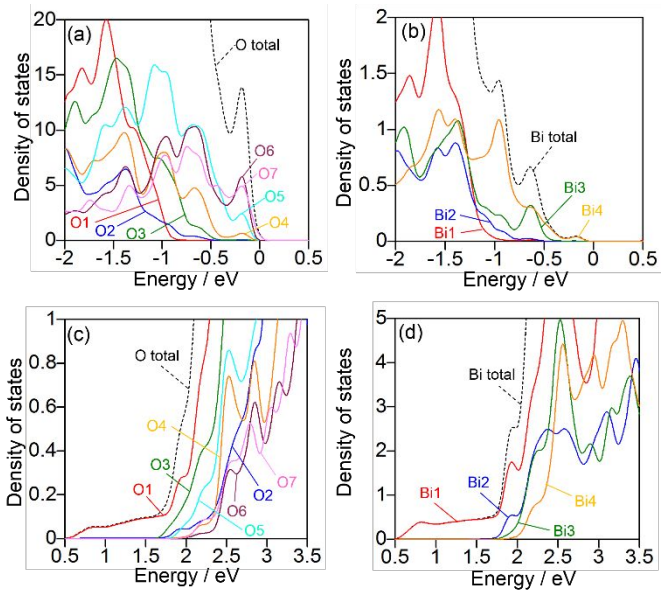

Fig. 10 PDOS around the VBM from (a) each O site and (b) Bi site, and around the CBM from (c) each O site and (d) Bi site in $Ba_3Bi_5Ti_5O_{20}Cl$ (**Ba-5**). See Fig. 5 for the detailed labelling.

The PDOS of **Ba-3** and **Ba-5** are shown in Fig. 9. Those at around their VBM comprise predominantly O-2p, not Cl-3p (Fig. 9a and 9d), similar to the n = 1–3 types of Sillén–Aurivillius phases.[17,18,22–24] As seen from the close-up around the VBM of **Ba-3** (Fig. 9b), the Bi-6s orbital also contributes to the VBM. In **Ba-5**, however, the contribution from Bi-6s is negligible (Fig. 9e). PDOS at around the CBM of both **Ba-3** and **Ba-5** are formed mainly by the Bi-6p orbital (Fig. 9c and 9f), while Ti-3d lies close to the CBM in **Ba-5**.

Fig. 10 depicts PDOS contributions from O and Bi site in **Ba-5** (see Fig. S17 for **Ba-3**). The O sites located in the center of

perovskite layer (i.e., O6 and O7) possess the greatest contribution to the VBM (Fig. 10a), while that in the fluorite layer (i.e., O1) shows the least one. Thus, there is contribution gradient from the center of the perovskite layer to the peripheral fluorite layer. A similar trend is also observed for the Bi sites (i.e., from Bi4 to Bi1; see Fig. 10b). In the PDOS of CBM, contributions from the O and Bi sites of the fluorite layer are much greater than those in the perovskite layer (Fig. 10c and 10d). These PDOS configurations may realize spatial separation between the VBM in the perovskite layer and CBM in the fluorite layer, which is advantageous for charge separation and following photocatalytic reactions.

Photocatalytic reaction

Photocatalytic reactions for H_2 and O_2 evolution were carried out in the presence of an electron donor (i.e., methanol) and an electron acceptor (i.e., Ag^+ or Fe^{3+}), respectively. Fig. 11 shows initial rates for H_2 evolution from an aqueous methanol solution under UV-visible light and O_2 evolution from an aqueous $AgNO_3$ or $Fe(ClO_4)_3$ solution under visible light. Interestingly, both H_2 and O_2 evolution rates were enhanced with increasing the number of perovskite layers. The reason is not clear at this stage, but the spatial separation between the perovskite (VBM) and fluorite layers (CBM), as proposed in PDOS, may cause charge separation, leading to higher photocatalytic activity.

As seen from time courses of O_2 evolution in Fig. S18, these materials exhibit O_2 evolution continuously, and noticeable deactivation are not observed. XRD patterns (Fig. S19) and SEM images (Fig. S20) are retained even after the photocatalytic reaction, thus these materials are stable during the photocatalytic reaction.

The apparent quantum efficiency (AQE) of O_2 evolution over **Ba-5** in the presence pf Fe^{3+} was determined to be 0.1% at 420 nm. This value is still lower than the case of n = 1 Bi_4NbO_8Cl that synthetically optimized and modified by a cocatalyst (2.5%).[44] However, there are room for being improved by various approaches making use of the extended perovskite layers such as cation substitutions, metal doping, as well as synthetic optimization and surface modifications.

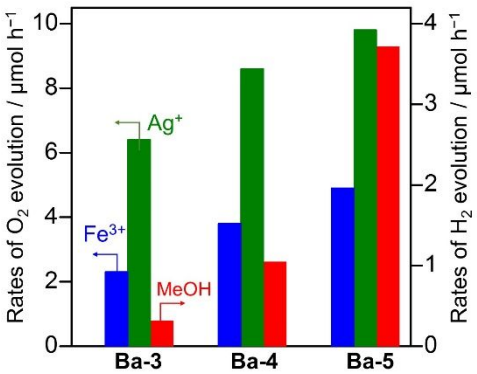

Fig. 11 Initial rates of photocatalytic O_2 or H_2 evolution on 100 mg of $BaBi_5Ti_3O_{14}Cl$ (**Ba-3**), $Ba_2Bi_5Ti_4O_{17}Cl$ (**Ba-4**) and $Ba_3Bi_5Ti_5O_{20}Cl$ (**Ba-5**) photocatalysts. (Blue and Green) O_2 evolution from aqueous solutions of $Fe(ClO_4)_3$ (5 mM, 120 mL, pH 2.3, adjusted by $HClO_4$) and $AgNO_3$ (10 mM, 120 mL), respectively, under visible light (400 < λ < 800 nm). (Red) H_2 evolution from a MeOH aqueous solution (20 vol%, 120 mL) under UV-visible light (300 < λ < 500 nm) with in-situ photodeposition of Pt cocatalyst (1 wt%).

Conclusion

We succeeded in synthesizing three new Sillén–Aurivillius oxychlorides $BaBi_5Ti_3O_{14}Cl$ (**Ba-3**), $Ba_2Bi_5Ti_4O_{17}Cl$ (**Ba-4**) and $Ba_3Bi_5Ti_5O_{20}Cl$ (**Ba-5**) with, respectively, triple-, quadruple- and quintuple-perovskite slabs, by employing the bricklaying synthesis. Their photocatalytic activities for H_2 or O_2 evolution were enhanced as increasing the number of the perovskite layers. The PDOS from each O and Bi site in **Ba-5** suggested spatial separation between perovskite layers (VBM) and fluorite layers (CBM), which may promote carrier separation. This discovery will provide a new design principle for developing efficient Sillén–Aurivillius oxyhalide photocatalysts for water splitting under visible light.

Experimental

Materials

Barium carbonate ($BaCO_3$, 99.99%), barium titanate ($BaTiO_3$, 99%), bismuth oxide (Bi_2O_3, 99.99%), bismuth oxychloride (BiOCl, 95.0%), hydrogen hexachloroplatinate hexahydrate ($H_2PtCl_6 \cdot 6H_2O$, 99.9%), iron(III) perchlorate *n*-hydrate ($Fe(ClO_4)_3 \cdot nH_2O$, 70% as anhydrous), methanol (CH_3OH, 99.8%), perchloric acid ($HClO_4$, 70% as assay), silver nitrate ($AgNO_3$, 99.8%), sodium sulfate (Na_2SO_4, 99.0%), strontium carbonate ($SrCO_3$, 99.99%), sulfuric acid (H_2SO_4, 0.5 M) and titanium oxide (TiO_2, 99.0%) were purchased from FUJIFILM Wako Chemicals. Strontium titanate ($SrTiO_3$, 99%) was purchased from Sigma-Aldrich. All chemicals were used as received, except $SrCO_3$, $BaCO_3$ and TiO_2 which were dried at 300 °C for 2 h before use.

Synthesis

All the samples in the present study were synthesized by solid-state reactions. Sillén phases $ABiO_2Cl$ (*A* = Sr, Ba) were synthesized from stoichiometric mixtures of ACO_3 and BiOCl. The mixtures were loaded in alumina crucibles and calcined in air at 700 °C for 10 h and 12 h for $BaBiO_2Cl$ and $SrBiO_2Cl$, respectively. An Aurivillius phase $Bi_4Ti_3O_{12}$ (n = 3) was prepared from a stoichiometric mixture of Bi_2O_3 and TiO_2 by heating at 800 °C for 1 h and subsequently 1000 °C for 10 h in an alumina crucible in air. Aurivillius phases $ABi_4Ti_4O_{15}$ (n = 4) were prepared from stoichiometric mixtures of $Bi_4Ti_3O_{12}$ and $ATiO_3$. The mixtures were heated at 800 °C for 1 h, and at 1000 °C for 10 h ($BaBi_4Ti_4O_{15}$) and at 1100 °C for 10 h ($SrBi_4Ti_4O_{15}$) in air. $A_2Bi_4Ti_5O_{18}$ (n = 5) were prepared from stoichiometric mixtures of $ABi_4Ti_4O_{15}$ and $ATiO_3$. The mixtures were heated at 800 °C for 1 h, and pelletized and heated at 1080 °C for 15 h three times ($Ba_2Bi_4Ti_5O_{18}$) and at 1100 °C for 15 h ($Sr_2Bi_4Ti_5O_{18}$) in air. Sillen–Auriviilius phases with n = 3–5 were tried to be synthesized by reactions between a Sillen phase $ABiO_2Cl$ and the corresponding Aurivillius phase, $Bi_4Ti_3O_{12}$ (n = 3), $ABi_4Ti_4O_{15}$ (n = 4) and $A_2Bi_4Ti_5O_{18}$ (n = 5), respectively. The mixture, including 10 mol% excess of the Sillen phase over the stoichiometric ratio, was pelletized, sealed in an evacuated quartz tube, and heated at 900 °C for 20 h.

Characterization

Laboratory powder X-ray diffraction (XRD; MiniFlex II, Rigaku, Cu Kα), scanning electron microscopy (SEM; NVision 40, Carl Zeiss-SIINT), scanning transmission electron microscopy (STEM; JEOL, JEM-ARM200CF) equipped with energy-dispersive X-ray spectroscopy (EDX), UV-visible diffuse reflectance spectroscopy (V-650, Jasco) were used for characterization. The adsorption

isotherm was measured by N_2 adsorption at liquid nitrogen temperature using automatic specific surface area measurement instrument (BELSORP-mini II, MicrotracBEL Corp.). The specific surface area was determined by Brunauer-Emmett-Teller (BET) method. Second harmonic generation (SHG) tests were performed using YAG:Nd laser (λ = 1064 nm) at 20 °C. Neutron powder diffraction (NPD; BT-1, NIST, US) for **Ba-3** was performed at room temperature (λ = 1.5401 Å using a Cu(311) monochromator). Synchrotron powder X-ray diffraction (SXRD; BL02B2, SPring-8, Japan) patterns were collected at room temperature (λ = 0.413269 Å for **Ba-3**; λ = 0.41943 Å for **Ba-4** and **Ba-5**). EXPO2014 and RIETAN-FP programs were used for indexing of diffraction peaks and Rietveld refinement, respectively.[45,46] Drawing crystal structures was performed by VESTA program.[47] Extreme ultra-violet light excited photoelectron spectroscopy (EUPS)[35,36] measurements were carried out. Laser-produced plasma of boron nitride (255.17 eV, 3 ns pulse duration) was used as an excitation source. In the EUPS system, photoelectrons emitted from samples were analyzed with a time-of-flight (TOF) analyzer with the work function of 4 eV. The pressure in the chamber was set to 10^{-7} Pa. In order to decrease surface contaminations, the measurements were carried out at 300 °C.

Electrochemical measurement

Mott−Schottky plots were collected in a three-electrode cell equipped with a Pt wire counter-electrode and a Ag/AgCl reference one in Na_2SO_4 aqueous solution (0.1 M, pH = 2.0, adjusted by 0.5 M H_2SO_4) by means of an electrochemical analyzer (VersaSTAT 4, Princeton Applied Research) with the amplitude of 10 mV and the frequencies of 500, 1000 and 2000 Hz. In order to prepare electrodes, a particulate sample with a small amount of water was coated on a fluorine-doped tin oxide (FTO) conductive substrate by a squeegee method and dried overnight at room temperature.

Calculation

The partial density of states (PDOS) of **Ba-3** and **Ba-5** were calculated by the density functional theory (DFT) using a plane-wave pseudopotential method by the Cambridge Serial Total Energy Package (CASTEP) program.[48] In the present study, the non-scalar relativistic effects and spin−orbital coupling were not employed. The energy was calculated by the generalized gradient approximation (GGA) of density functional theory (DFT) proposed by Perdew, Brurke and Ernzerhof (PBE). In the structural model of **Ba-3**, we adopted the $2a \times 2b \times 1c$ supercell and the setting where Bi/Ba1 site was perfectly occupied by Bi (i.e., Bi: 1, Ba: 0), and Bi/Ba2 and Bi/Ba 3 sites were occupied by three Bi and one Ba of four atoms (i.e., Bi: 3/4, Ba: 1/4). As for **Ba-5**, we employed the $\sqrt{2}a \times \sqrt{2}a \times 1c$ supercell and the setting where Bi/Ba1 site was also fully occupied by Bi, and Bi/Ba2, Bi/Ba 3 and Bi/Ba4 sites were occupied by one Bi and one Ba of two atoms (i.e., Bi: 1/2, Ba: 1/2). For the calculation of **Ba-3** and **Ba-5**, each cut-off energy was set to 630 eV and 700 eV, respectively, and the k-point meshes were set to 2 × 2 × 1 and 5 × 5 × 1, respectively. Before the PDOS calculation, the geometry optimization based on the Broyden−Fletcher−Goldfarb−Shanno (BFGS) algorithm was carried out.

Photocatalytic reactions

Photocatalytic reactions were performed in a Pyrex overhead-irradiation-type reaction vessel connected to a closed gas-circulation system which was degassed and purged with Ar gas. A Xe lamp (LAMP HOUSE R300-3J, Eagle engineering, 300 W) equipped with a cold mirror (CM-2, Kenko) was used as UV-visible light source (300 < λ < 500 nm). The Xe lamp equipped with both a cold mirror (CM-1, Kenko) and a cut-off filter (L-42, HOYA) was used as a visible light irradiation (400 < λ < 800 nm). The evolved gases were analyzed using an online gas chromatography (GC-8A, Shimadzu, thermal conductivity detector, 5 Å molecular sieve column packing) with Ar as the carrier gas.

A photocatalyst (100 mg) was used for each photocatalytic reaction. For the photocatalytic H_2 evolution, the photocatalyst was suspended in an aqueous methanol solution (20 vol%, 120 mL) including H_2PtCl_6 as a precursor of a Pt cocatalyst (1 wt%) and irradiated with UV-visible light. As for the photocatalytic O_2 evolution, the photocatalyst was suspended in a aqueous solution of $AgNO_3$ (10 mM, 120 mL) or $Fe(ClO_4)_3$ (5 mM, 120 mL, pH = 2.3 adjusted by $HClO_4$) and irradiated with visible light. The apparent quantum efficiency (AQE) for O_2 evolution was measured by using monochromatic light (420 nm) emitted from the Xe lamp equipped with both a CM-1 cold mirror and a bandpass filter (λ = 420 ± 5 nm, ASAHI). The AQE was calculated by the equation as follows;

$$\mathrm{AQE}\ (\%) = (4 \times R/I) \times 100 \quad (1)$$

where *R* and *I* represent the rate of O_2 evolution and the rate of incident photons. The total number of incident photons was measured to be 101.6 mW by a power meter with a photodiode.

Author Contributions

D. O.: Conceptualization, Investigation, Methodology, Resources, Visualization, Writing - original draft, Writing - review & editing. **H. S.:** Writing - review & editing. **K. O.:** Investigation, Writing - review & editing. **R. S.:** Writing - review & editing. **O. T.:** Writing - review & editing. **Y. I.:** Investigation. **K. N.:** Investigation. **H. K.:** Writing - review & editing, Supervision, Funding acquisition. **R. A.:** Writing - original draft, Writing - review & editing, Supervision, Funding acquisition, Project administration.

Conflicts of interest

There are no conflicts to declare.

Acknowledgements

This work was supported by JST CREST (JPMJCR1421), JSPS Core-to-Core Program (JPJSCCA20200004), JSPS KAKENHI (JP20H00398) in Grant-in-Aid for Scientific Research (A), JSPS KAKENHI (JP16H06438) in Grant-in-Aid for Scientific Research on Innovative Area "Mixed Anion" and JSPS KAKENHI (JP17H06439) in Scientific Research on Innovative Area "Innovations for Light-Energy Conversion (I^4LEC)". A part of this work was supported by Advanced Characterization Platform and AIST Nanocharacterization Facility (ANCF) Platform as a program of "Nanotechnology Platform" of the Ministry of Education, Culture, Sports, Science and Technology (MEXT), Japan, Grant Number JPMXP09A20KU0355 and JPMXP09A20AT0001, respectively. We are also grateful to Mr. Takaaki Toriyama of Kyushu University for his helpful support in STEM analysis, and to Dr. Toshihisa Tomie, Mr. Tomoaki Ishitsuka and Dr. Nobuyuki Matsubayashi of AIST for their helpful support in EUPS measurement. SXRD experiments were carried out at the BL02B2 of SPring-8 with the approval of the

Japan Synchrotron Radiation Research Institute (JASRI) (Proposal No. 2019B1764 and 2020A1686). We acknowledge the support of the National Institute of Standards and Technology, U. S. Department of Commerce, in providing the neutron research facilities used in this work.

References

1 A. Kudo and Y. Miseki, *Chem. Soc. Rev.*, 2009, **38**, 253−278.
2 R. Abe, *J. Photochem. Photobiol. C*, 2010, **11**, 179−209.
3 T. Takata and K. Domen, *ACS Energy Lett.*, 2019, **4**, 542−549.
4 F. E. Osterloh, *Chem. Mater.*, 2008, **20**, 35−54.
5 X. B. Chen, C. Li, M. Gräzel, R. Kostecki and S. S. Mao, *Chem. Soc. Rev.*, 2012, **41**, 7909 −7937.
6 K. Maeda and K. Domen, *J. Phys. Chem. C*, 2007, **111**, 7851−7861.
7 Q. Wang and K. Domen, *Chem. Rev.*, 2020, **120**, 919−985.
8 H. Kageyama, K. Hayashi, K. Maeda, J. P. Attfield, Z. Hiroi, J. M. Rondinelli and K. R. Poeppelmeier, *Nat. Commun.*, 2018, **9**, 772.
9 D. S. Bhachu, S. J. A. Moniz, S. Sathasivam, D. O. Scanlon, A. Walsh, S. M. Bawaked, M. Mokhtar, A. Y. Obaid, I. P. Parkin, J. Tangb and C. J. Carmalt, *Chem. Sci.*, 2016, **7**, 4832−4841.
10 Z. Ran, X. Wang, Y. Li, D. Yang, X. Zhao, K. Biswas, D. J. Singh and L. Zhang, *npj Computational Mater.*, 2018, **14**, 4.
11 J. Olchowka, H. Kabbour, M. Colmont, M. Adlung, C. Wickleder and O. Mentre, *Inorg. Chem.*, 2016, **55**, 7582−7592.
12 J. Sun, Q. Sun, A. Plewa, Y. Wang, L. He, F. Zheng, C. Chen, W. Zajac, J. Molenda, K. Zeng and L. Lu, *Angew. Chem. Int. Ed.*, 2020, **59**, 8991−8997.
13 K. Ogawa, Y. Wakisaka, H. Suzuki, O. Tomita and R. Abe, *ACS Appl. Mater. Interfaces.*, 2020, DOI:10.1021/acsami.0c14964
14 J. Shang, W. Hao, X. Lv, T. Wang, X. Wang, Y. Du, S. Dou, T. Xie, D. Wang and J. Wang, *ACS Catalysis*, 2014, **4**, 954−961.
15 P. K. Prajapati and S. L. Jain, *Dalton Trans.*, 2019, **48**, 4941−4948.
16 A. Nakada, D. Kato, R. Nelson, H. Takahira, M. Yabuuchi, M. Higashi, H. Suzuki, M. Kirsanova, N. Kakudou, C. Tassel, T. Yamamoto, C. M. Brown, R. Dronskowski, A. Saeki, A. Abakumov, H. Kageyama and R. Abe, *J. Am. Chem. Soc.*, DOI: 10.1021/jacs.0c10288.
17 H. Fujito, H. Kunioku, D. Kato, H. Suzuki, M. Higashi, H. Kageyama and R. Abe, J. *Am. Chem. Soc.*, 2016, **138**, 2082−2085.
18 H. Kunioku, M. Higashi, O. Tomita, M. Yabuuchi, D. Kato, H. Fujito, H. Kageyama and R. Abe, *J. Mater. Chem. A*, 2018, **6**, 3100−3107.
19 D. Ávila-Brande, Á. R. Landa-Cánovas, and L. C. Otero-Díaz, *Chem. Mater.*, 2007, **19**, 323-328.
20 A. Pandeya, G. Naresha and T. K. Mandal, *Solar Energy Materials & Solar Cells*, 2017, **161**, 197–205.
21 A. M. Kusainova, W. Zhou, J. T. S. Irvine and P. Lightfoot, *J. Solid State Chem.*, 2002, **166**, 148−157.
22 A. Nakada, M. Higashi, T. Kimura, H. Suzuki, D. Kato, H. Okajima, T. Yamamoto, A. Saeki, H. Kageyama and R. Abe, *Chem. Mater.*, 2019, **31**, 3419−3429.
23 D. Ozaki, H. Suzuki, A. Nakada, M. Higashi, O. Tomita, H. Kageyama and R. Abe, *Chem. Lett.*, 2020, **49**, 978−981.
24 D. Ozaki, H. Suzuki, O. Tomita, Y. Inaguma, K. Nakashima, H. Kageyama and R. Abe, *J. Photochem. Photobiol. A: Chem.*, 2020, DOI:10.1016/j.jphotochem.2020.113095
25 H. G. Kim, D. W. Hwang and J. S. Lee, *J. Am. Chem. Soc.*, 2004, **126**, 8912−8913.
26 H. Wakayama, K. Utimula, T. Ichibha, R. Kuriki, K. Hongo, R. Maezono, K. Oka and K. Maeda, *J. Phys. Chem. C*, 2018, **122**, 26506−26511.
27 R. Kuriki, T. Ichibha, K. Hongo, D. Lu, R. Maezono, H. Kageyama, O. Ishitani, K. Oka and K. Maeda, *J. Am. Chem. Soc.*, 2018, **140**, 6648−6655.
28 H. Suzuki, H. Kunioku, M. Higashi, O. Tomita, D. Kato, H. Kageyama and R. Abe, *Chem. Mater.*, 2018, **30**, 5862−5869.
29 D. O. Charkin, V. S. Akinfiev, A. M. Alekseeva, M. Batuk, A. M. Abakumov and S. M. Kazakov, *Dalton Trans.*, 2015, **44**, 20568–20576.
30 D. O. Charkin, D. N. Lebedev and S. M. Kazakov, *Russ. J. Inorg. Chem.* 2012, **57**, 917–922.
31 J. Cao, V. Koval, H. Zhang, Y. Lin, J. Wu, N. Meng, Y. Li, Z. Li, H. Zhang and H. Yan, *J. Eur. Ceram. Soc.*, 2019, **39**, 1042−1049.
32 A. Kitada, Y. Tsujimoto, T. Yamamoto, Y. Kobayashi, Y. Narumi, K. Kindo, A. A. Aczel, G. M. Luke, Y. J. Uemura, Y. Kikuchi, Y. Ueda, K. Yoshimura. Y. Ajiro and H. Kageyama, *J. Solid State. Chem.*, 2012, **185**, 10−17.
33 B. Aurivillius, *Chemica Scripta*, 1984, **23**, 143−156.
34 A. Nakada. A. Saeki, M. Higashi, H. Kageyama and R. Abe, *J. Mater. Chem. A*, 2018, **6**, 10909−10917.
35 T. Tomie, T. Ishitsuka, T. Ootsuka and H. Ota, *AIP Conf. Proc.*, 2011, **1395**, 148−153.
36 Y. Kawaguchi, F. Sasaki, H. Mochizuki, T. Ishitsuka, T. Tomie, T. Ootsuka, S. Watanabe, Y. Shimoi, T. Yamao and S. Hotta, *J. Appl. Phys.*, 2013, **113**, 083710.
37 A. M. Kusainova, S. Y. Stefanovich, J. T. S. Irvine and P. Lightfoot, *J. Mater. Chem.*, 2002, **12**, 3413−3418.
38 A. Walsh, D. J. Payne, R. G. Egdell and G. W. Watson, *Chem. Soc. Rev.*, 2011, **40**, 4455−4463.
39 R. A. Armstrong and R. E. Newnham, *Mat. Res. Bull.*, 1972, **7**, 1025−1034.
40 X. Zhou and H. Dong, *J. Phys. Chem. C*, 2017, **121**, 20662−20672.
41 H. Suzuki, S. Kanno, M. Hada, R. Abe and A. Saeki, *Chem. Mater.*, 2020, **32**, 4166-4173.
42 R. D. Shannon, *Acta Crystallogr. A*, 1976, **32**, 751−767.
43 K. H. Xue, L. R. C. Fronseca and X. S. Miao, *RSC. Adv.*, 2017, **7**, 21856−21868.
44 K. Ogawa, A. Nakada, H. Suzuki, O. Tomita, M. Higashi A. Saeki, H. Kageyama and R. Abe, *ACS Appl. Mater. Interfaces*, 2019, **11**, 5642−5650.
45 A. Altomare, C. Cuocci, C. Giacovazzo, A. Moliterni, N. Corriero and A. Falcicchio, *J. Appl. Cryst.*, 2013, **46**, 1231−1235.
46 F. Izumi and K. Momma, *Solid State Phenom*, 2007, **130**, 15−20.
47 K. Momma and F. Izumi, *J. Appl. Cryst.*, 2011, **44**, 1272−1276.
48 S. J. Clark, M. D. Segall, C. J. Pickard, P. J. Hasnip, M. J. Probert, K. Refson and M. C. Payne, *Z. Kristallogr.*, 2005, **220**, 567−570.

ARTICLE